Materials Science and Engineering B 298 (2023) 116858

Contents lists available at ScienceDirect

Materials Science & Engineering B

journal homepage: www.elsevier.com/locate/mseb

Effect of boron incorporation on the structural, morphological, and spectral properties of $CdNb_2O_6$:Dy^{3+} phosphor synthesized by molten salt process

Mustafa İlhan [a,*], Mete Kaan Ekmekçi [b], Lütfiye Feray Güleryüz [c]

[a] Department of Environmental Engineering, Faculty of Engineering, Marmara University, Maltepe 34854, İstanbul, Turkey
[b] Marmara University, Department of Chemistry, Faculty of Science, Marmara University, Kadıkoy 34722, Istanbul, Turkey
[c] Department of Tobacco Technology Engineering, Manisa Celal Bayar University, Akhisar 45200, Manisa, Turkey

ARTICLE INFO

Keywords:
$CdNb_2O_6$
Boron effect
Grain morphology
Luminescence
Decay time

ABSTRACT

The effect of boron addition on the structural, morphologic and spectral properties was investigated by using xDy^{3+} (x = 0.5, 3, 6 mol%) doped, and xDy^{3+}, yB^{3+} (y = 0, 5, 15, 25 mol%) co-doped $CdNb_2O_6$ powders produced by molten salt method. X-ray diffractions (XRD) of all Dy^{3+} doped, and B^{3+}, Dy^{3+} co-doped samples showed that they retained the single-phase structure. The homogeneous dissolution of the Dy^{3+} doping without forming an impurity phase in the structure can be attributed to the flux effect of the molten salt process and boron doping. Scanning electron microscopy (SEM) micrographs of the B^{3+}, Dy^{3+} co-doped grains showed that the effect of boron promotes grain growth and prismatic-like grain shape. Photoluminescence (PL) emissions of the phosphors with the excitation of 351.9 nm were monitored by the $^4F_{9/2}\rightarrow{}^6H_{15/2}$, $^4F_{9/2}\rightarrow{}^6H_{13/2}$, and $^4F_{9/2}\rightarrow{}^6H_{11/2}$ transitions. PL excitations and a broad peak at 275 nm originating from the $O^{2-}\rightarrow Nb^{5+}$ band transition were observed with the emission of 577.9 nm. The PL emissions of Dy^{3+}, B^{3+} co-doped phosphors increased about two fold compared to Dy^{3+} doped samples. The increase in PL may be related to the increased presence of luminescence centers at or near grain surface due to the decreasing surface area (SA)/volume (V) ratio as the growth of B^{3+} co-doped grains and the transformation from rod-like to prismatic-like shape. The increased Dy^{3+} presence led to a decrease in observed lifetime, while the B^{3+} increase did not cause any change. The study may provide a different perspective for the understanding and controlling of grain morphology and the luminescence relation for RE-doped phosphors.

1. Introduction

The phosphors activated with trivalent rare earth ions (RE^{3+}) have led to promising developments in applications such as LEDs (light emitting diodes), solid-state lasers, optical communication and temperature sensing, while distinguishing optical features like long luminescence lifetimes, high photostability, and narrow emission bandwidths its specifications arouse great interest [1–9]. Morphological features such as grain size and grain shape are essential parameters in the development of the structural properties of luminescent materials, and their control is important for improving spectral properties. The vitrification of boron plays an effective role in enhancing crystallization, lowering the melting temperature, and improving structural and optical properties [10–15]. There are studies investigating the effect of boron addition on structural and spectral properties of different host materials, and these studies mostly emphasize the relationship between crystallinity and luminescence. However, there are relatively few studies that refer to the relationship between morphology and luminescence, such as $SrTa_2O_6$:Eu^{3+},B^{3+} [11], $Ba_{0.88}Mg_{0.93}Al_{10}O_{16.96}$:$Eu^{3+}$, B^{3+} [12], Gd_2O_3:Eu [13], $SrAl_2O_4$:Eu,Dy [14], $SrAl_2O_4$:Eu^{2+} [15].

The AB_2O_6 (A = Cd^{2+}, Co^{2+}, Ca^{2+}, Mg^{2+}, Mn^{2+}, Sr^{2+}, etc; B = Nb^{5+}, Ta^{5+}) orthorhombic columbite structure consists of octahedra encircled by six oxygens, in which the divalent A and pentavalent B cations are located at the center. The octahedra of AO_6 and BO_6 create zig-zag sequences independently by sharing edges. These sequences are linked together by sharing corners in the order of the AO_6-BO_6-BO_6 sequences [16–18]. The $CdNb_2O_6$ compound has been investigated in terms of its structural [19–22], photocatalytic [19], thermodynamic [20], and luminescence [21,22] properties. In the synthesis of ceramics, the diffusion kinetics and reaction rates tend to be slow in low-temperature processes due to restricted thermal activation. To overcome these limitations, one well-known approach is to increase the heat treatment

* Corresponding author.
E-mail address: mustafa.ilhan@marmara.edu.tr (M. İlhan).

https://doi.org/10.1016/j.mseb.2023.116858
Received 20 June 2023; Received in revised form 1 September 2023; Accepted 4 September 2023
Available online 12 September 2023

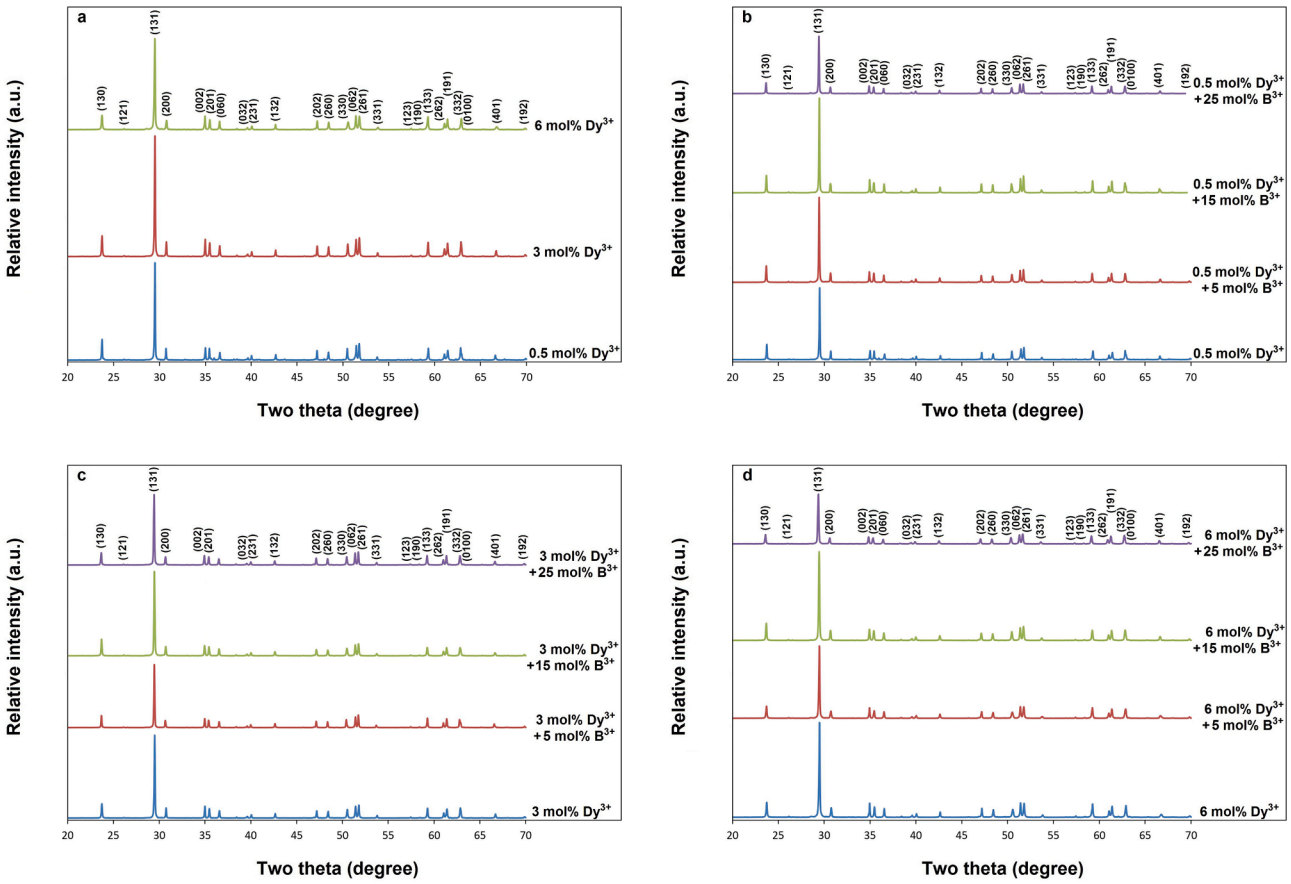

Fig. 1. XRD results of (a) 0.5, 3, 6 mol% Dy^{3+} doped $CdNb_2O_6$ samples, and (b) 0.5 mol% Dy^{3+}, yB^{3+}, (c) 3 mol% Dy^{3+}, yB^{3+}, (d) 6 mol% Dy^{3+}, yB^{3+} ($y = 0$, 5, 15, 25 mol%) co-doped $CdNb_2O_6$ samples.

temperature, which enhances reaction and mass transport rates, leading to shorter process durations. The solid state synthesis based on mixture of oxides is an example of this strategy. On the other hand, molten salt synthesis capitalizes on the superior mass transport rates achievable in a melt, allowing for synthesis to be conducted at moderate temperatures while maintaining a reasonable rate of progress [23,24]. In addition, this method is one of the favorite production methods owing to some supremacies such as low sintering temperatures, strong compositional homogeneity, and short reaction time [25,26].

In the study, the structural, morphological and spectral properties of Dy^{3+} doped and Dy^{3+}, B^{3+} co-doped $CdNb_2O_6$ phosphors produced by the molten salt method were studied in terms of their luminescence, decay, and grain morphology properties. Although there are studies on luminescence and grain morphology in the literature, detailed studies on the particle size/particle shape and luminescence relation are relatively scarce, so the study may contribute to future research in the field. The

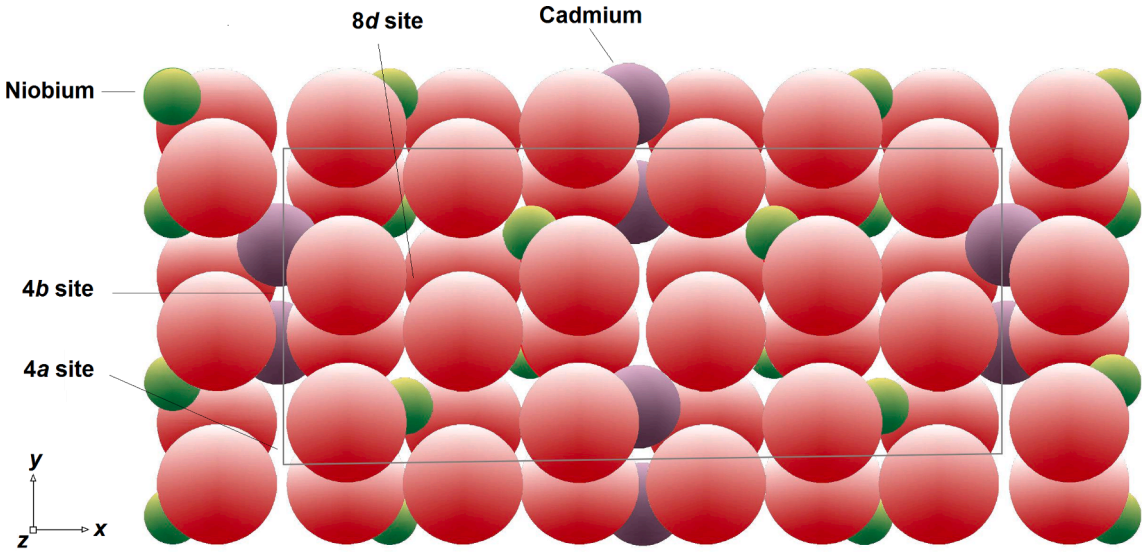

Fig. 2. Schematic illustration of $CdNb_2O_6$ crystal structure.

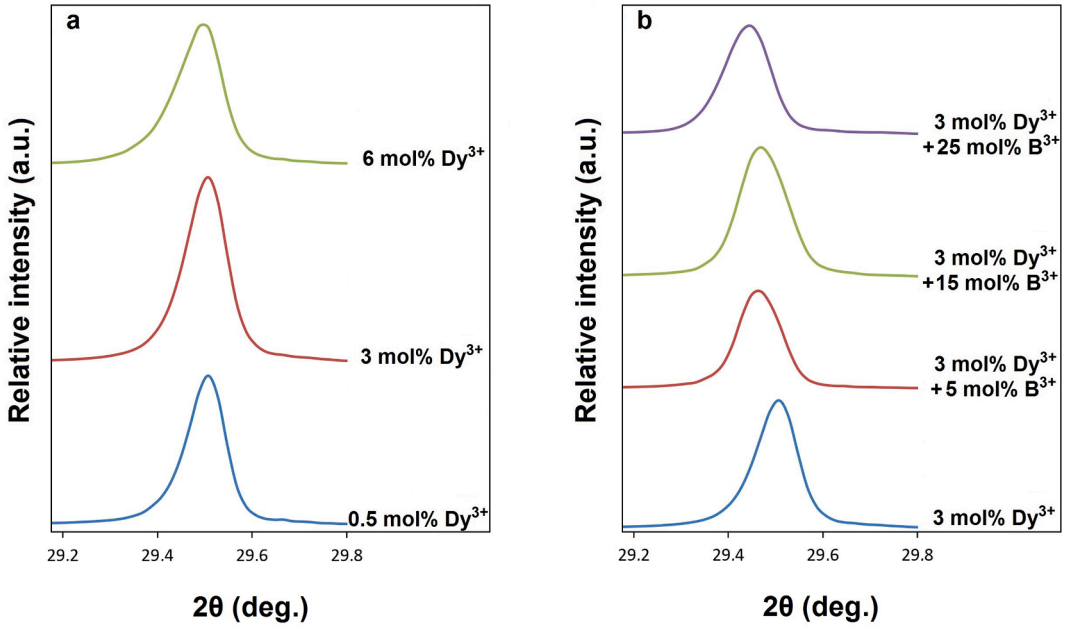

Fig. 3. Shift of XRD two theta peak (1 3 1) to lower angles for (a) 0.5, 3, 6 mol% Dy^{3+} doped $CdNb_2O_6$ samples, (b) 3 mol% Dy^{3+}, yB^{3+} ($y = 0$, 5, 15, 25 mol%) co-doped $CdNb_2O_6$ samples.

structural and spectral analyses of the ceramic powders were performed by XRD, SEM, XPS, PL, and decay time investigations.

2. Experimental

The $CdNb_2O_6$:xDy^{3+}, yB^{3+} ($x = 0.5$, 3, 6 mol%, $y = 0$, 5, 15, 25 mol %) phosphor powders were fabricated via the molten salt method. The $Cd(NO_3)_2{\cdot}4H_2O$ (Sigma-Aldrich, 99%), Nb_2O_5 (Alfa Aesar, 99.9%), H_3BO_3 (Kimyalab, %99.9), and Dy_2O_3 (Alfa Aesar, 99.9%) were used in the synthesis process. The salt mixture of Li_2SO_4:Na_2SO_4 was used as a flux, where the molar ratio salt to salt is 0.635:0.365. The salt-to-oxide weight ratio was set at 1:1 for the experiment. To ensure homogeneity, the starting materials were mixed and ground thoroughly in an agate mortar. Subsequently, dysprosium oxide (Dy_2O_3) and boric acid (H_3BO_3) were added to the powder mixture, which was then mixed and ground again in the agate mortar to enhance homogeneity. For the heat treatment process, a sufficient amount of the mixture was weighted and calcined in an Al crucible at 900 °C for 4 h. To remove ionic salts from the oxides, the sintered powders were washed using pure water. The availability of SO_4^{2-} ions was confirmed through qualitative reactions.

The X-ray diffractometer (D2 PHASER, Bruker Corp., Germany) with Cu-Kα radiation was used to identify the crystalline phase of the powders. Scanning electron microscopy (FEG-SEM; XL 30S, Philips Corp., Netherlands) was employed for investigating the grain morphology of the samples after Au coating. The Thermo-Scientific Al-Kα model X-ray photoelectron spectroscopy (XPS) device was employed for elemental analysis. PL results were acquired using an Edinburgh Instruments FLS920 fluorescence spectrometer, equipped with a 450 W ozone-free xenon lamp. Lifetime data were obtained using the time-correlated single-photon counting (TCSPC) system. The PL analysis was conducted at room temperature.

3. Results and discussions

3.1. XRD, SEM and XPS results

Fig. 1(a-d) shows the XRD findings of 0.5, 3, 6 mol% Dy^{3+} doped and xDy^{3+}, yB^{3+} ($x = 0.5$, 3, 6 mol% and $y = 5$, 15, 25% mol% B^{3+}) co-doped $CdNb_2O_6$ powder samples, respectively. The XRD patterns of the samples revealed the presence of an orthorhombic columbite structure (JCPDS card no: 38-1428), belonging to space group *Pbcn*(60). The schematic illustration of $CdNb_2O_6$ crystal structure is shown in Fig. 2. There are three vacant octahedral sites labeled as 4*a*, 4*b*, and 8*d*, where the 4*a* sites being the most favorable for Dy^{3+} occupancy [27,28]. In Fig. 1a, there is no any minor phase in the XRD patterns of Dy^{3+} doped samples. The absence of the impurity phase can be attributed to the successful insertion of Dy^{3+} ions to the most suitable 4*a* sites, with the advantage of the diffusion process improved in molten salt synthesis. In Fig. 1(b-d), XRD patterns of xDy^{3+}, yB^{3+} ($x = 0.5$, 3, 6 mol% and $y = 5$, 15, 25% mol% B^{3+}) co-doped samples exhibiting $CdNb_2O_6$ single phase can be explained by the dissolution of boron in the orthorhombic columbite crystal structure [22]. Based on the co-doped Dy^{3+} and B^{3+} ions being placed in the lattice as interstitial atoms, the presence of Dy^{3+} and B^{3+} ions can alter the charge balance within the structure by introducing additional positive charges into the lattice. Fig. 3(a, b) shows XRD peaks (1 3 1) for xDy^{3+} ($x = 0.5$, 3, 6 mol%) doped and 3 mol % Dy^{3+}, yB^{3+} ($y = 0$, 5, 15, 25 mol%) co-doped samples, respectively.

Table 1
Cell parameters of $CdNb_2O_6$:xDy^{3+}, yB^{3+} ($x = 0.5$, 3, 6 mol%, $y = 0$, 5, 15, 25 mol%) powders.

Sample		Lattice parameters			
Dy^{3+} (mol%)	B^{3+} (mol%)	*a* (Å)	*b* (Å)	*c* (Å)	*V* (Å^3)
0.5	0	5.8206	14.6798	5.1355	438.81
	5	5.8237	14.7392	5.1370	440.94
	15	5.8242	14.7351	5.1307	440.32
	25	5.8275	14.7541	5.1386	441.81
3	0	5.8133	14.6928	5.1390	438.94
	5	5.8316	14.7220	5.1330	440.68
	15	5.8206	14.7210	5.1409	440.50
	25	5.8252	14.7499	5.1365	441.33
6	0	5.8097	14.7200	5.1373	439.33
	5	5.8181	14.7192	5.1433	440.46
	15	5.8242	14.7351	5.1428	441.36
	25	5.8389	14.7918	5.1460	444.45

Table 2
Crystallite sizes of $CdNb_2O_6$:xDy^{3+}, yB^{3+} (x = 0.5, 3, 6 mol%, y = 0, 5, 15, 25 mol%) powders.

Dy^{3+} (mol%)	B^{3+} (mol%)			
	0	5	15	25
0.5	77.76	74.09	73.06	72.46
3	69.91	71.44	63.71	63.25
6	62.03	56.18	54.13	49.08

Accordingly, the shift in XRD peaks to the lower two theta angles is due to the increased positive charge causing more expansion in the lattice constant. The lattice parameters calculated using (130), (131), and (200) reflections are given in Table 1, where increased Dy^{3+} and B^{3+} presence led to an increase in the lattice constant. The lattice volume from 0.5 to 6 mol% Dy^{3+} changed to 438.81 and 439.33 $Å^3$, respectively, and it reached a maximum value of 444.45 $Å^3$ for 6 mol% Dy^{3+}, 25 mol % B^{3+} co-doped sample. The cell parameters of $CdNb_2O_6$ are reported as $a = 5.8480$ Å, $b = 14.7817$ Å, $c = 5.1419$ Å, $V = 444.49$ $Å^3$, $Z = 4$ [29]. In the study, the lattice volume is approximately 1.3% smaller than the reported in the literature for the 0.5 mol% Dy^{3+} doped sample and approached the reported value with the increase in Dy^{3+} and B^{3+}. In Fig. 3(a,b), the broadening XRD (131) peaks of the samples show that the crystallinity affected due to the increase of both Dy^{3+} and B^{3+}. The average crystallite sizes of the samples can be found using Eq. (1) derived by Scherrer [5]:

$$D = \frac{k \cdot \lambda}{B \cdot \cos\theta} \quad (1)$$

where D is the particle size (nm), k is a constant (assumed to be 0.9), CuKα denotes the wavelength ($\lambda = 0.15406$), B is the full width at half maximum in radians. The symbol θ represents the angle in degrees between the incident and diffracted beams. The average crystallite sizes calculated from XRD peaks with the strongest intensity [30] for reflections of the (130), (131), and (261) are tabulated in Table 2. The crystallite sizes of the Dy^{3+} doped samples from 0.5 to 6 mol% changed to 77.76 and 62.03 nm, respectively, while they varied in the range of 77.76–72.46 and 62.03–49.08 nm for 0.5 and 6 mol% Dy^{3+}, yB^{3+} (y = 0, 5, 15, 25 mol%) co-doped series, respectively. The decrease in crystallite size was closely related to the presence of both Dy^{3+} and B^{3+}, and the

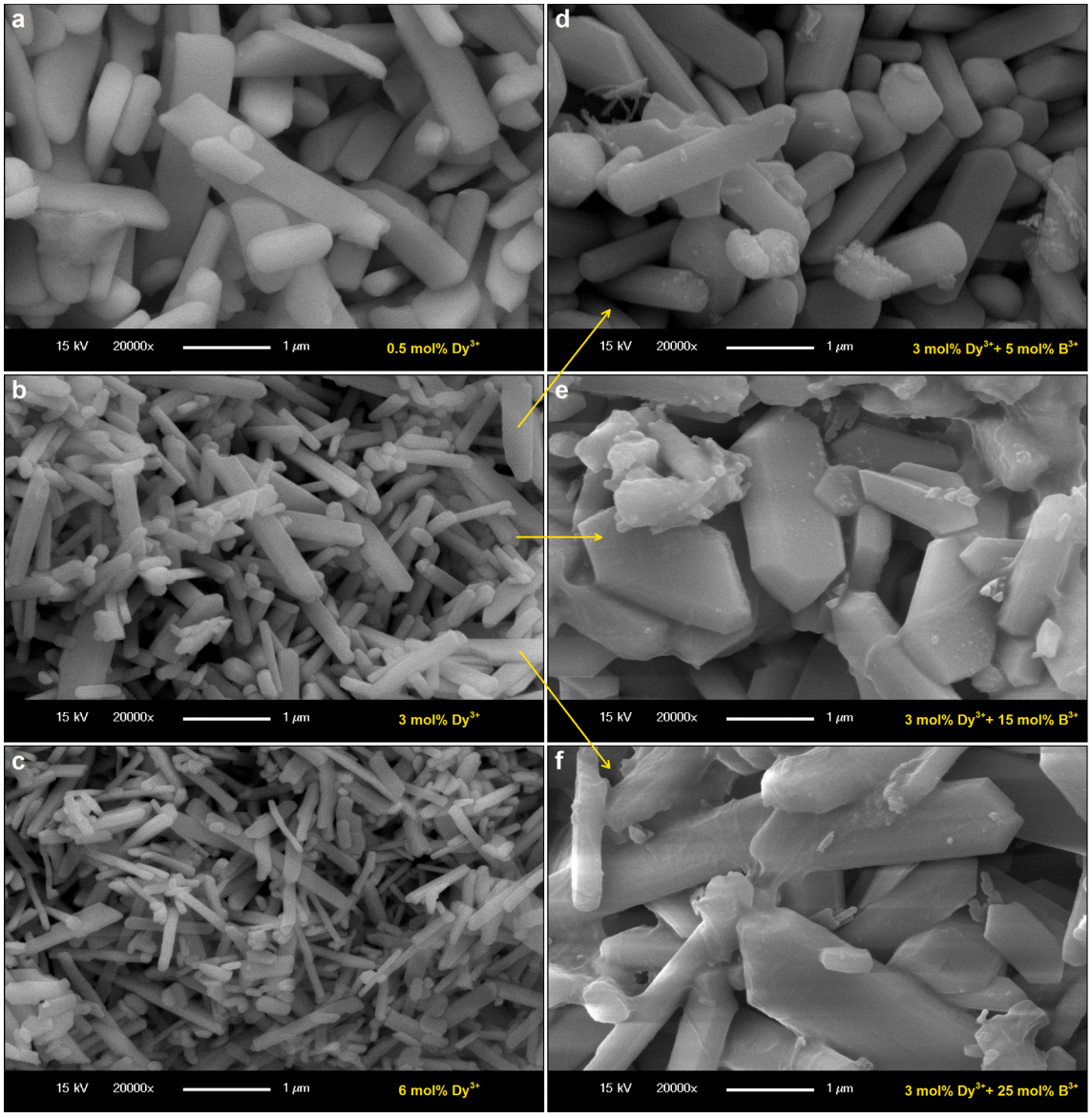

Fig. 4. SEM micrographs for (a) 0.5, (b) 3, (c) 6 mol% Dy^{3+} doped $CdNb_2O_6$ samples, and 3 mol% Dy^{3+} and different concentrations B^{3+} co-doped $CdNb_2O_6$ samples (d) 5 mol%, (e) 15 mol%, (f) 25 mol%, under 15 kV accelerating voltage at 20.000× magnifications.

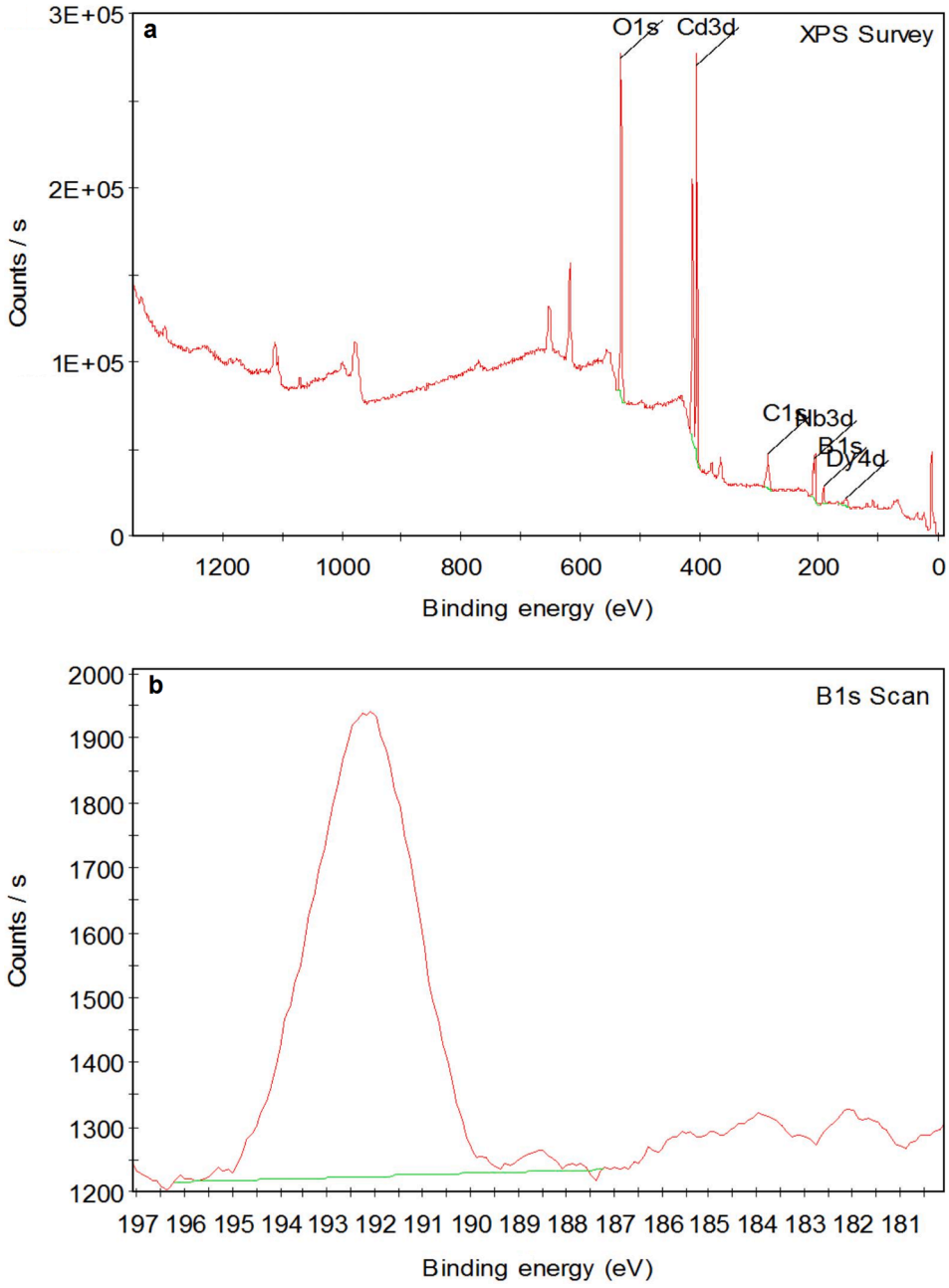

Fig. 5. XPS results of 3 mol% Dy^{3+}, 15 mol% B^{3+} co-doped $CdNb_2O_6$ sample, (a) XPS survey, (b) B1s.

decrease was more with increasing B^{3+} concentration at high Dy^{3+} concentrations. As seen in Table 2, the increased B^{3+} led to a slight decrease in crystallinity for 0.5 mol% Dy^{3+}, yB^{3+} ($y = 0$, 5, 15, 25 mol%) co-doped series, whereas the decrease was higher in 6 mol% Dy^{3+}, yB^{3+} ($y = 0$, 5, 15, 25 mol%) co-doped series. The decrease in crystallite size may be ascribed to the increased distortion in the lattice due to the increased presence of Dy^{3+} and B^{3+} ions. Besides, as consistent with previously reported studies [31–35], the high boron doping causes a decrease in crystallinity by deteriorating the charge balance in the structure.

Fig. 4(a–f) show SEM micrographs Dy^{3+} doped, and Dy^{3+}, B^{3+} co-doped ceramic powders. In Fig. 4(a-c), SEM micrographs of 0.5, 3, and 6 mol% Dy^{3+} doped $CdNb_2O_6$ samples revealed a rod-like morphology of the orthorhombic crystal. The thicknesses of the grains for 0.5, 3, and 6 mol% Dy^{3+} doped series varied in the range of 0.3–0.8, 0.2–0.6 and 0.05–0.3 μm, while lengths of the same series changed between 0.8–3.5, 0.6–3.1 and 0.5–2.2 μm, respectively. The decrease in grain size as Dy^{3+} increases is due to the inhibitory effect on crystallinity caused by the expansion of the lattice symmetry, as indicated in the XRD findings. Fig. 4(d–f) shows SEM micrographs for 3 mol% Dy^{3+}, yB^{3+} ($y = 5$, 15, 25 mol%) co-doped samples, respectively. As seen from the micrographs, boron doping promotes agglomeration, grain growth, and prismatic-like shape in grains. This effect can be clearly observed for 3 mol% Dy^{3+} doped sample (Fig. 4b) compared to Dy^{3+}, B^{3+} co-doped samples (Fig. 4(d-f)). The thickness and lengths for 3 mol% Dy^{3+}, 25 mol% B^{3+} co-doped sample are between 0.5–1.8 and 0.9–4.0 μm, respectively. In the case of comparison of Dy^{3+} doped and Dy^{3+}, B^{3+} doped samples in terms of grain size and grain shape, the increase in B^{3+} transforms the grains from rod shape to prismatic shape by increasing the grain size, while the increase in Dy^{3+} has the opposite effect. The survey and B1s of XPS (X-ray photoelectron spectroscopy) for the 3 mol % Dy^{3+}, 15 mol% B^{3+} co-doped sample is given in Fig. 5(a,b),

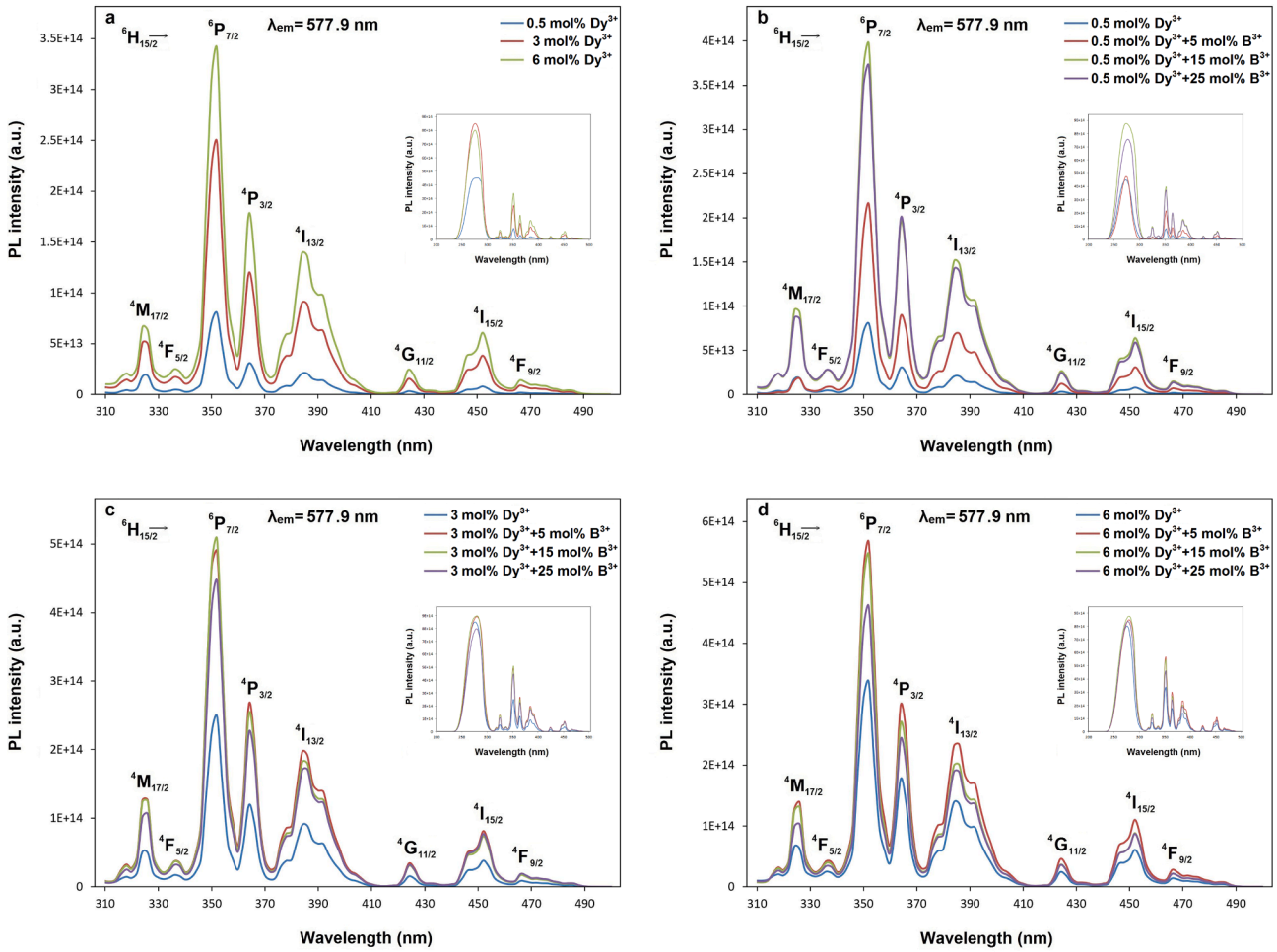

Fig. 6. PL excitation spectra and the O^{2-}–Nb^{5+} transitions (inset figures) for (a) 0.5, 3, 6 mol% Dy^{3+} doped $CdNb_2O_6$ phosphors, and (b) 0.5 mol% Dy^{3+}, yB^{3+}, (c) 3 mol% Dy^{3+}, yB^{3+}, (d) 6 mol% Dy^{3+}, yB^{3+} (y = 0, 5, 15, 25 mol%) co-doped $CdNb_2O_6$ phosphors corresponding to 677.9 nm emission.

respectively. As seen in Fig. 5a, the XPS result shows the presence of Dy, O, Cd, Nb and B in the structure. The binding energies for O 1s, Cd 3d, and Nb 3d were identified at 531.51, 405.06, and 206.71 eV to belong to cadmium niobate oxide, respectively. In addition, the peak of 153.97 eV represents the dysprosium with Dy 4d. In Fig. 5b, the B1s has a binding energy of 192.50 eV, indicating the presence of boron in the structure, as evidenced by the broad spectrum observed in the range of approximately 190–195 eV. The elemental and fully oxidized (B_2O_3) forms of boron have binding energies of 187.2 eV [36] and 193.0 eV [37,38], respectively. Hence, the wide range of B1s associated with interstitial B atoms can be attributed to the existence of fully oxidized forms containing oxygen within the structure.

3.2. *Photoluminescence of $CdNb_2O_6$:xDy^{3+}, and $CdNb_2O_6$:xDy^{3+}, yB^{3+} phosphors*

Fig. 6(a-d) shows PL excitation spectra of $CdNb_2O_6$:xDy^{3+} (x = 0.5, 3, 6 mol%) doped and $CdNb_2O_6$:xDy^{3+}, yB^{3+} (x = 0.5, 3, 6 mol%, y = 5, 15, 25 mol%) co-doped phosphors recorded from the emission of 577.9 nm. The excitations of all the phosphors were labeled as the $^6H_{15/2}\rightarrow{}^4M_{17/2}$, $^6H_{15/2}\rightarrow{}^4F_{5/2}$, $^6H_{15/2}\rightarrow{}^6P_{7/2}$, $^6H_{15/2}\rightarrow{}^4P_{3/2}$, $^6H_{15/2}\rightarrow{}^4I_{13/2}$, $^6H_{15/2}\rightarrow{}^4G_{11/2}$, $^6H_{15/2}\rightarrow{}^4I_{15/2}$ and $^6H_{15/2}\rightarrow{}^4F_{9/2}$ transitions, which are related to the intra-configurational (f-f) transitions of Dy^{3+}. The inset figures in Fig. 6(a-d) show the peaks associated with the O^{2-}–Nb^{5+} transition, which has a wide band and maxima of the 274–280 nm range. In different studies, the excitation and emission bands of $CdNb_2O_6$ are reported as 272 [39,40], 275 nm [41], and 460 nm [39–41], respectively, and they are consistent with the findings of the study. PL emissions of $CdNb_2O_6$:xDy^{3+}, and $CdNb_2O_6$:xDy^{3+}, yB^{3+} phosphors monitored by the $^4F_{9/2}\rightarrow{}^6H_{13/2}$ strong transition and $^4F_{9/2}\rightarrow{}^6H_{15/2}$, $^4F_{9/2}\rightarrow{}^6H_{11/2}$ transitions under excitation of 351.9 nm are shown in Fig. 7(a-d). The PL emissions increased approximately two fold at 5 mol% B^{3+} concentration for Dy^{3+}, B^{3+} co-doped phosphors compared to Dy^{3+} doped samples. In the luminescence of RE activators, low crystal field symmetry, and good crystallinity are generally believed to be advantageous [42]. Accordingly, the asymmetry ratios ($^4F_{9/2}\rightarrow{}^6H_{13/2}$/ $^4F_{9/2}\rightarrow{}^6H_{15/2}$) of Dy^{3+}, B^{3+} co-doped phosphors are slightly higher compared to Dy^{3+} doped samples (Fig. 8), so the decrease in the local symmetry of Dy^{3+} ions may slightly contribute to PL. As mentioned before, it has been observed that boron doping has no effect on crystallization, and there are similar studies in the literature regarding the increase in luminescence despite the decreasing crystallinity with boron doping [34,35]. However, it was observed that the presence of boron affected the grain size and grain shape. The effects of these morphological parameters on luminescence have been studied by different researchers. Kim and Kang [43] emphasized that increasing grain size leads to an increase in luminescence due to fewer non-luminescent centers formed near the grain surface. Shan et al [44] studied in detail the effect of grain shape on luminescence that differently shaped nanocrystals with the same surface area (SA)/volume (V) ratios can have different lattice energies and multiphonon relaxation processes, where surface effects are crucial. Moreover, it has been suggested that phosphor with a spherical grain morphology has better spectral properties such as low light scattering, bright luminescence, and higher definition

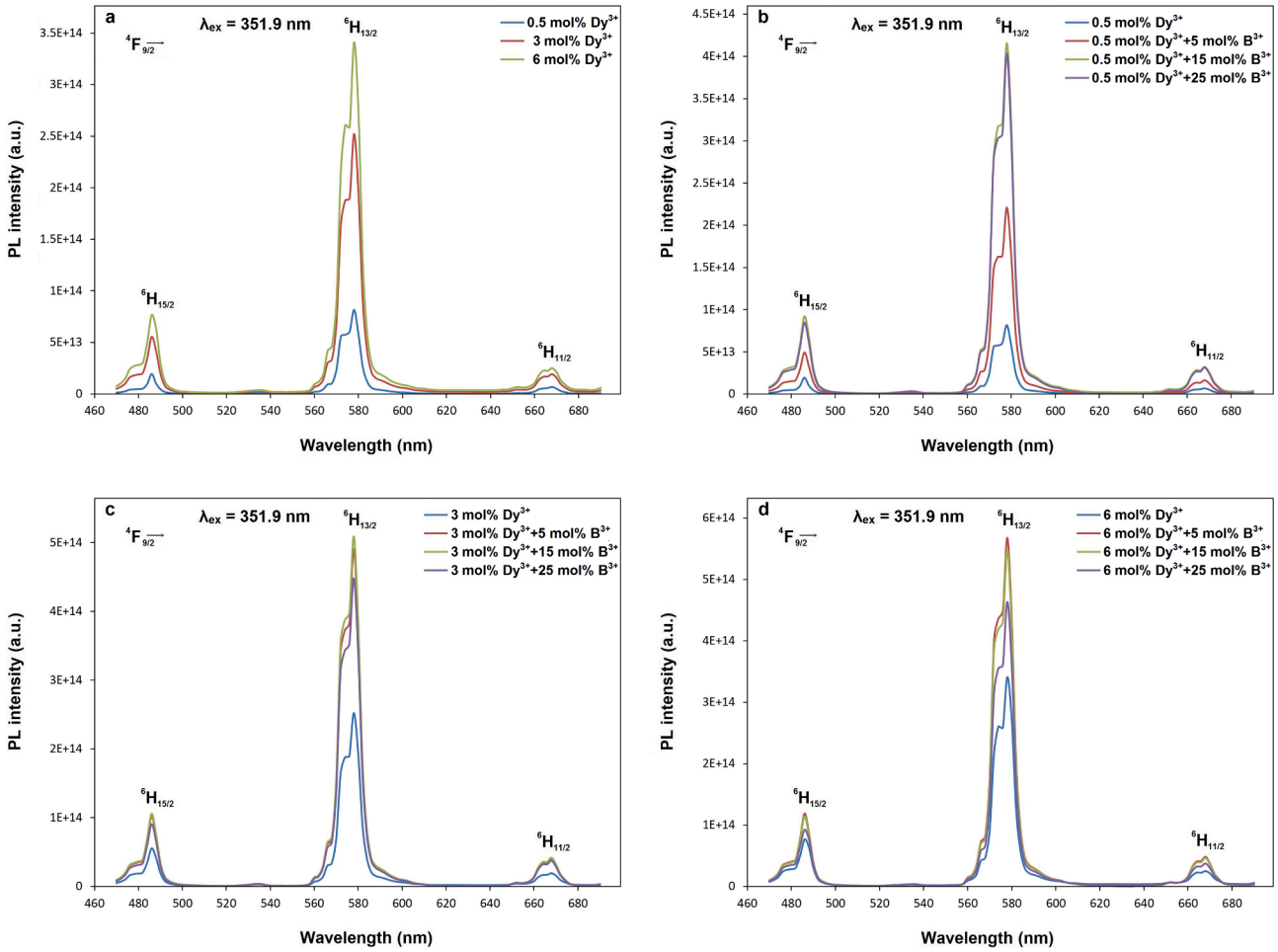

Fig. 7. PL emission spectra for (a) 0.5, 3, 6 mol% Dy^{3+} doped $CdNb_2O_6$ phosphors, and (b) 0.5 mol% Dy^{3+}, yB^{3+}, (c) 3 mol% Dy^{3+}, yB^{3+}, (d) 6 mol% Dy^{3+}, yB^{3+} (y = 0, 5, 15, 25 mol%) co-doped $CdNb_2O_6$ phosphors with excitation of 351.9 nm.

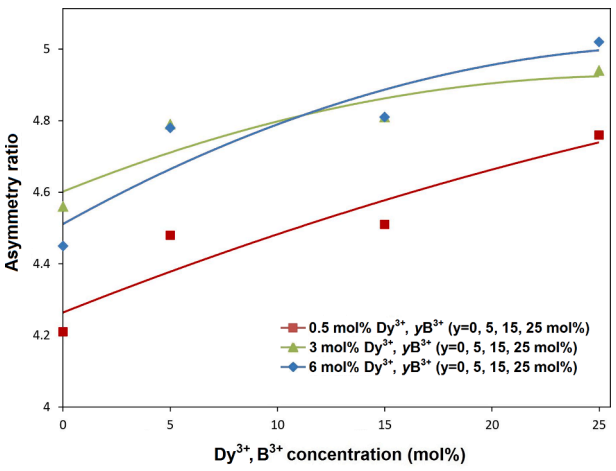

Fig. 8. Asymmetry ratio variation of $CdNb_2O_6$:xDy^{3+}, yB^{3+} (x = 0.5, 3, 6 mol %, y = 0, 5, 15, 25 mol%) phosphors depending on concentration.

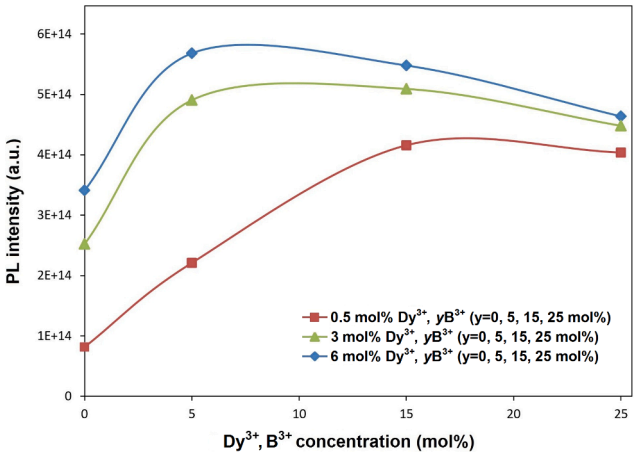

Fig. 9. PL intensity change of $^4F_{9/2}$→$^6H_{13/2}$ transition of $CdNb_2O_6$:xDy^{3+}, yB^{3+} (x = 0.5, 3, 6 mol%, y = 0, 5, 15, 25 mol%) phosphors depending on concentration.

due to its high packing density [45,46]. Accordingly, the increase in luminescence can be attributed to the decrease in multiphonon relaxation processes due to the decrease in SA/V ratio as Dy^{3+}, B^{3+} co-doped grains grow and their transformation from rod-like form to prismatic shape. Although there is a decrease in crystallinity, the increase in luminescence is probably due to the vitrification effect of boron, which leads to agglomeration of grains and increased grain size, decreased surface roughness and ultimately reduced SA/V. So, when considered from this aspect, boron doping decreases the effect of crystallinity on luminescence to some extent. Fig. 9 shows the variation in PL emissions depending on the increase of Dy^{3+} and B^{3+} concentrations. The concentration quenching was not observed with Dy^{3+} increase. However, a

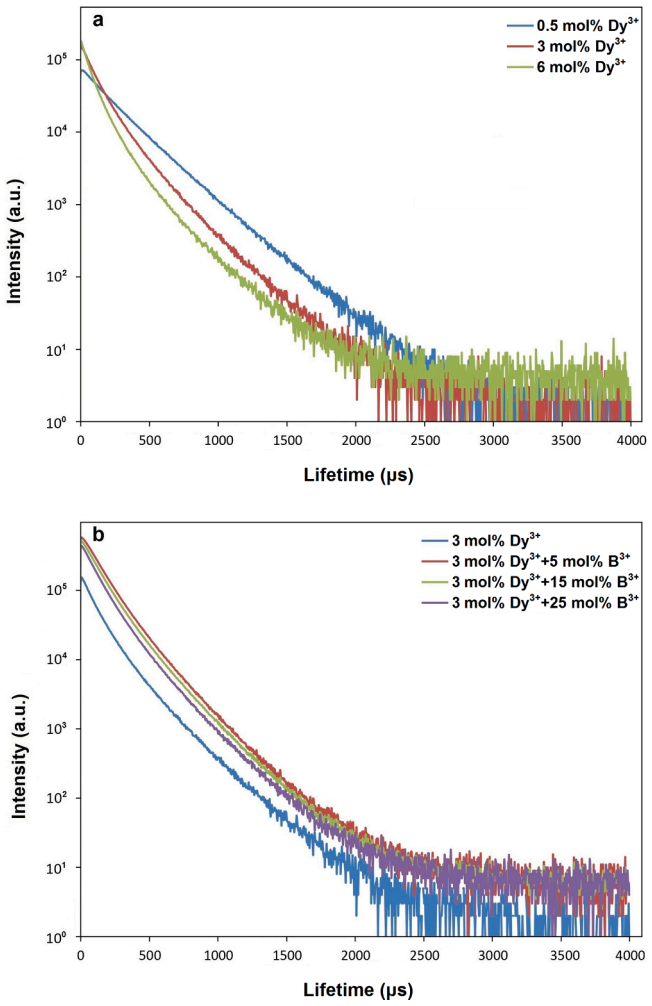

Fig. 10. Decay curves of (a) 0.5, 3, 6 mol% Dy^{3+} doped $CdNb_2O_6$ phosphors, and (b) 3 mol% Dy^{3+}, yB^{3+}, (y = 5, 15, 25 mol%) co-doped $CdNb_2O_6$ phosphors.

slight decrease occurred with the B^{3+} increase in emissions. The PL intensity decreased at 15, 25 mol% B^{3+} for 6 mol% Dy^{3+} co-doped series, whereas the emission decrease occurred at 25 mol B^{3+} concentration for 0.5 and 3 mol Dy^{3+} co-doped series. As seen in Fig. 9, the 0.5 mol% Dy^{3+} doped phosphor series showed the highest emission increase at 5, 15, and 25 mol% B^{3+} concentrations, whereas the 6 mol% Dy^{3+} doped series exhibited the small increase at the same B^{3+} concentrations. It is likely that the less affected crystallite of 0.5 Dy^{3+}, yB^{3+} (y = 5, 15, 25 mol%) co-doped series resulted in more luminescence enhancement.

Fig. 10(a, b) shows the decay curves of $^4F_{9/2}\rightarrow{}^6H_{13/2}$ transition (577.9 nm) under 351.9 nm excitation for Dy^{3+} doped and Dy^{3+}, B^{3+} co-doped phosphors, respectively. The two-exponential decay curves can be defined using the Eq. (2):

$$I_t = I_0 + I_1 exp\frac{-t}{\tau_1} + I_2 exp\frac{-t}{\tau_2} \quad (2)$$

where I_t represents the PL intensity, t stands for the time elapsed after excitation, I_0 denotes the background, while I_1 and I_2 represent the luminescence intensities associated with the long lifetime (τ_1) and short lifetime (τ_2), respectively. Hence, the average or observed lifetime (τ) can be determined using Eq. (3) [11,47]:

$$\tau = \frac{I_1\tau_1^2 + I_2\tau_2^2}{I_1\tau_1 + I_2\tau_2} \quad (3)$$

The bi-exponential decays for $x$$Dy^{3+}$ (x = 0.5, 3, 6 mol%) doped and

Table 3
Long (τ_1), short (τ_2) lifetimes, and observed lifetimes (τ) of $CdNb_2O_6$:xDy^{3+} (x = 0.5, 3, 6 mol%) and $CdNb_2O_6$:xDy^{3+}, yB^{3+} (x = 3 mol%, y = 5, 15, 25 mol%) phosphors.

$CdNb_2O_6$:xDy^{3+}				$CdNb_2O_6$:$3Dy^{3+}$, yB^{3+}			
Phosphor (mol%)	τ_1 (ms)	τ_2 (ms)	τ (ms)	Phosphor (mol%)	τ_1 (ms)	τ_2 (ms)	τ (ms)
0.5Dy^{3+}	0.259	0.146	0.229	3Dy^{3+}, 5B^{3+}	0.219	0.110	0.149
3Dy^{3+}	0.213	0.088	0.139	3Dy^{3+}, 15B^{3+}	0.214	0.104	0.145
6Dy^{3+}	0.208	0.076	0.129	3Dy^{3+}, 25B^{3+}	0.210	0.098	0.142

3 mol% Dy^{3+}, yB^{3+} (y = 0, 5, 15, 25 mol%) co-doped phosphors are summarized in Table 3. The observed lifetimes in the range of 0.5–6 mol % Dy^{3+} decreased from 0.229 to 0.129 ms, respectively. However, there is no decrease occurred in the observed lifetimes for 3 mol% Dy^{3+}, yB^{3+} (y = 0, 5, 15, 25 mol%) co-doped phosphors, and changed as 0.139, 0.149, 0.145, 0.142 ms, respectively. In Table 3, the long (τ_1) and short (τ_2) lifetimes for Dy^{3+} doped samples varied between 0.259 and 208 and 0.146–0.076 ms, respectively, while the τ_1 and τ_2 lifetimes of 3 mol% Dy^{3+}, yB^{3+} (y = 0, 5, 15, 25 mol%) co-doped phosphors changed between 0.213 and 210 and 0.088–0.098 ms, respectively. The long lifetime (τ_1) is associated with RE^{3+} ions in the inside of the particle, and short lifetime (τ_2) is related to RE^{3+} ions close to the surface and/or on the surface of the particle [48]. Accordingly, for Dy^{3+} doped phosphors, the decrease in τ_1 lifetime with increasing Dy^{3+} may be attributed to the reduction of luminescence centers inside the grain resulting from decreasing crystallite or increased structural defects. The decreased τ_2 lifetime is associated with the grain size reduction or increased SA/V ratio, which decreases the activation of Dy^{3+} centers on the grain surface. However, the decrease in τ_2 lifetime is more than τ_1. In addition to the decrease in grain size, the increased SA/V ratio is likely to further reduce τ_2 lifetime as the grain shape becomes more rod-like. For 3 mol% Dy^{3+}, yB^{3+} (y = 0, 5, 15, 25 mol%) co-doped samples, the slightly changed τ_1 lifetime may be associated with the less effected crystallinity. The decrease in crystallinity is 25.36% in the range of 0.5–6 mol Dy^{3+}, while it is 10.53% for the 3 mol% Dy^{3+}, yB^{3+} (y = 0, 5, 15, 25 mol%) series. The τ_2 lifetimes from 3 mol% Dy^{3+}, to 3 mol% Dy^{3+}, 5 mol% B^{3+} phosphor changed to 0.088 and 0.110 ms, respectively. The increase in τ_2 lifetime indicates the activation of Dy^{3+} luminescence centers on the grain surfaces due to the decreased SA/V ratio. As well known, the distance between RE ions associated with non-radiative energy transfer and structural defects are important factors in luminescence process. Firstly, an increase in Dy^{3+} concentration will make the energy transfer process more frequent and there will be a decrease in the distance and decay time of Dy^{3+} ions, so an increase in non-radiative transitions will be more likely. Secondly, the increased presence of Dy^{3+} will cause effects on structural and morphological features such as decreased crystallinity and reduction/elongation of the grains, resulting in a slowdown and decrease in the energy transfer process. In conclusion, on the basis of the decay results supporting the PL results, the increased luminescence of $CdNb_2O_6$:Dy^{3+},B^{3+} phosphor may be attributed to the enhanced morphological features and/or decreased SA/V ratio that optimize the energy transfer between Dy^{3+} luminescence centers. Also, less affected crystallinity at lower doping ratios will contribute more to this phenomenon than higher doping ratios.

The CIE (Commission Internationale de I'Eclairage) chromaticity coordinates of $CdNb_2O_6$:xDy^{3+}, yB^{3+} (x = 0.5, 3, 6 mol%, y = 0, 5, 15, 25 mol%) co-doped phosphors under excitation of 351.9 nm are shown in Fig. 11. CIE chromaticity coordinates (x, y) all the phosphors located in yellow region are tabulated in Table 4. Further, McCamy Eq. (4) was utilized to calculate the color correlated temperature (CCT) values, aiming to assess the quality of white light [49]:

$$CCT = -449n^3 + 3525n^2 - 6823n + 5520.33 \quad (4)$$

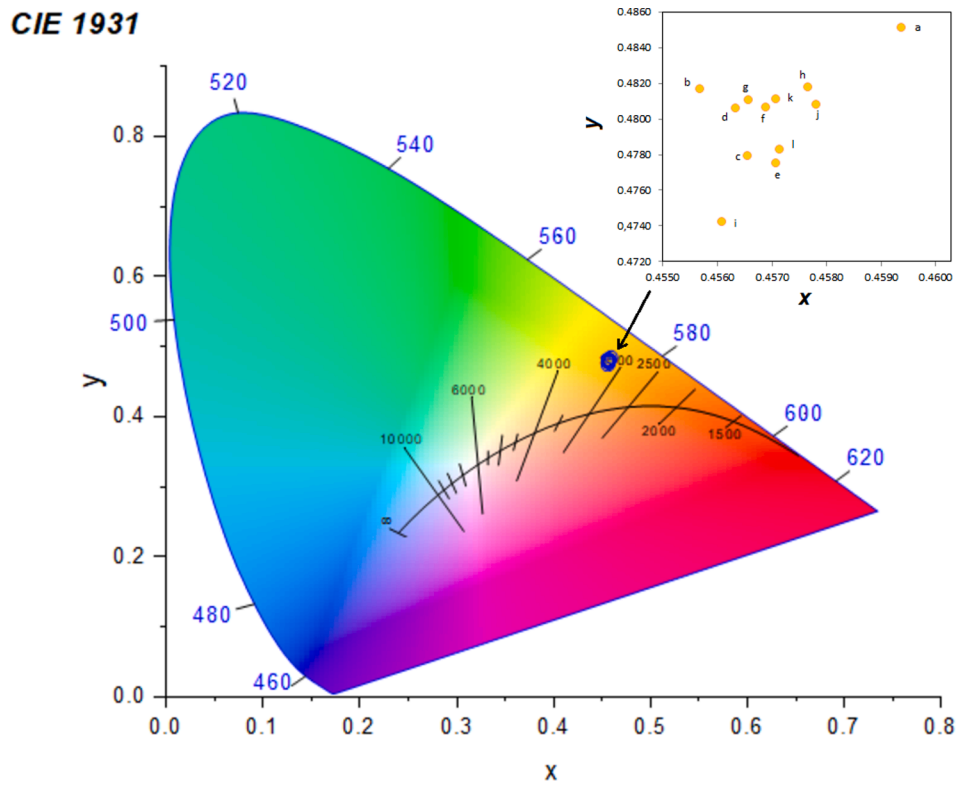

Fig. 11. CIE diagram and detailed (*x*,*y*) coordinates (inset figure) of $CdNb_2O_6$:xDy^{3+}, yB^{3+} (x = 0.5, 3, 6 mol%, y = 0, 5, 15, 25 mol%) phosphors.

Table 4
CIE coordinates, and correlated color parameters of $CdNb_2O_6$:xDy^{3+}, yB^{3+} (x = 0.5, 3, 6 mol%, y = 0, 5, 15, 25 mol%) phosphors with the excitation of 351.9 nm.

Sample		Phosphor symbolized in CIE diagram	CIE coordinates		CCT
Dy^{3+} (mol %)	B^{3+} (mol %)		*x*	*y*	(K)
0.5	0	a	0.4594	0.4851	3219
	5	b	0.4557	0.4817	3251
	15	c	0.4566	0.4779	3218
	25	d	0.4563	0.4806	3238
3	0	e	0.4571	0.4775	3210
	5	f	0.4569	0.4806	3232
	15	g	0.4566	0.4811	3240
	25	h	0.4577	0.4818	3230
6	0	i	0.4561	0.4742	3208
	5	j	0.4578	0.4808	3225
	15	k	0.4571	0.4811	3238
	25	l	0.4572	0.4783	3221

where $n = (x–x_e)/(y–y_e)$ is the inverse slope line, and $x_e = 0.332$ and $y_e = 0.186$. In general, the recommended range for CCT parameters is 3500 to 6500 K, although a range of 3000 to 7800 K is also considered acceptable. The phosphors exhibited CCT values within the range of 3208–3251 K are presented in Table 4. The estimated CCT data for all samples in the warm light region is appropriate for household lighting purposes. Fig. 12 shows the UV photographs of $CdNb_2O_6$:Dy^{3+} and $CdNb_2O_6$:Dy^{3+}, B^{3+} phosphors under 254 nm which is compatible with yellow region in CIE diagram. In the UV-lamp photographs, the colors obtained from all the samples became brighter with increasing Dy^{3+} and B^{3+} concentrations. As consistent with PL emission changes given in Fig. 9, the 6 mol% Dy^{3+}, 5 mol% B^{3+} co-doped phosphor with the highest PL emission intensity has the highest brightness.

4. Conclusion

Dy^{3+} doped and Dy^{3+}, B^{3+} co-doped $CdNb_2O_6$ powders were synthesized using the molten salt method, which allows for a lower temperature and better homogeneity compared to other conventional methods. XRD results revealed the single orthorhombic columbite structure of $CdNb_2O_6$ having the *Pbcn(60)* space group symmetry for all the powder samples. The increase in Dy^{3+} and B^{3+} concentration led to an increase in cell volume and it caused a decrease in crystallinity. SEM examinations of the samples showed that Dy^{3+} increase led to a rod-like morphology, while the boron increase promoted grain growth and prismatic-like morphology. XPS results of 3 mol% Dy^{3+}, 15 mol% B^{3+} co-doped sample showed that boron atoms were in completely oxidized forms with the oxygen in the structure. PL emissions were observed correspondingly to the $^4F_{9/2}$→$^4H_{15/2}$, $^4F_{9/2}$→$^4H_{13/2}$, $^4F_{9/2}$→$^4H_{11/2}$ and $^4F_{9/2}$→$^4H_{9/2}$ transitions. The emission intensity of Dy^{3+}, B^{3+} co-doped phosphors increased nearly twofold compared to Dy^{3+} doped samples. Depending on the boron increase, a slight decrease in PL emissions was observed for 6 mol% Dy^{3+}, 5 mol% B^{3+} co-doped phosphors, while concentration quenching did not occur with the Dy^{3+} increase. The increase in PL was associated with the increased presence of Dy^{3+} centers close to and at the grain surface depending on the decreasing SA/V ratio as the B^{3+} doped grains grew larger and transformed from rod-like to prismatic-like shape. The increase in Dy^{3+} concentration led to a decrease in the lifetimes, while a slight increase was observed in the decays with increased B^{3+} concentration. The increasing short component showed that the activation of Dy^{3+} centers at and near the grain surface and the luminescence enhances due to the increase of boron, while the decreased short component with the increase in Dy^{3+} indicated the decreased activation in Dy^{3+} centers due to the decreased grain size and rod-like grain shape morphology. The phosphors under UV lamp excitation showed a brighter appearance with increasing Dy^{3+} and B^{3+} concentrations, consistent with PL emissions. The research

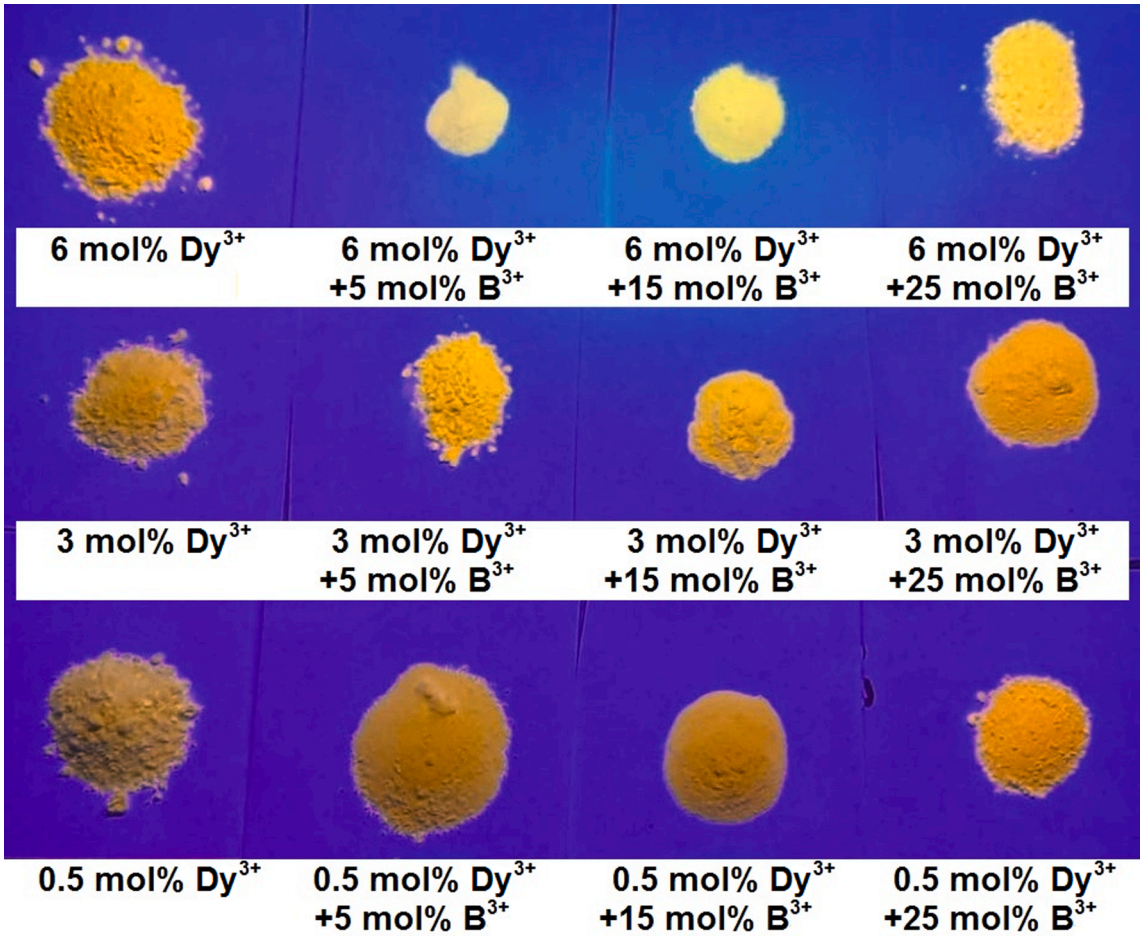

Fig. 12. UV lamp photographs of $CdNb_2O_6$:xDy^{3+}, yB^{3+} (x = 0.5, 3, 6 mol%, y = 0, 5, 15, 25 mol%) phosphors under 254 nm.

could offer a new perspective on future research concerning the controlling and tunability of grain morphology and luminescence in RE-doped phosphors.

Declaration of Competing Interest

The authors declare that they have no known competing financial interests or personal relationships that could have appeared to influence the work reported in this paper.

Data availability

Data will be made available on request.

References

[1] G.R. Banjare, D.P. Bisen, N. Brahme, C. Belodhiya, Mater. Sci. Eng. B 263 (2021), 114882.
[2] G.V. Kanmani, V. Ponnusamy, G. Rajkumar, S.M.M. Kennedy, J. Mater. Sci.: Mater. Electron. 34 (2023) 765.
[3] Y. Shi, C. Dong, J. Shi, Mater. Sci. Eng. B 228 (2018) 28–37.
[4] R. Song, H. Li, H. Zhang, H. Tang, X. Tang, J. Yang, H. Zhao, J. Zhu, Appl. Mater. Today 30 (2023), 101712.
[5] S. Gökçe, İ.Ç. Keskin, M.İ. Katı, R. Kibar, A. Çetin, Y.T. Arslanlar, J. Lumin. 261 (2023), 119883.
[6] J. Huang, Q. Li, D. Chen, Mater. Sci. Eng. B 172 (2010) 108–113.
[7] W. Park, R.Y. Lee, C.J. Summers, Y.R. Do, H.G Yang, Mater. Sci. Eng. B 78 (2000) 28–31.
[8] R. Lohan, A. Kumar, M.K. Sahu, A. Mor, V. Kumar, N. Deopa, A.S. Rao, J. Mater. Sci.: Mater. Electron. 33 (2022) 16606–16620.
[9] H. You, X. Wu, X. Zeng, G. Hong, C.H. Kim, C.H. Pyun, C.H. Park, Mater. Sci. Eng. B 86 (2001) 11–14.
[10] Y. Huang, Q. Feng, Y. Yang, H.J. Seo, Phys. Lett. A 336 (2005) 490–497.
[11] M. İlhan, L.F. Güleryüz, RSC. Adv. 13 (2023) 12375.
[12] A. Dulda, D.S. Jo, W.J. Park, T. Masaki, D.H. Yoon, J. Ceram. Process. Res. 10 (2009) 811–816.
[13] Y.C. Kang, H.S. Roh, S.B. Park, Jpn. J. Appl. Phys. 39 (2000) L31–L33.
[14] V. Vitola, I. Bite, D. Millers, A. Zolotarjovs, K. Laganovska, K. Smits, A. Spustaka, Ceram. Int. 46 (2020) 26377–26381.
[15] S. Yoon, J. Bierwagen, M. Trottmann, B. Walfort, N. Gartmann, A. Weidenkaff, H. Hagemann, S. Pokrant, J. Lumin. 167 (2015) 126–131.
[16] C.A. dos Santos, L.I. Zawislak, E.J. Kinast, V. Antonietti, J.B.M. da Cunha, Braz. J. Phys. 31 (2001) 616–631.
[17] R.C. Pullar, J. Am. Ceram. Soc. 92 (2009) 563–577.
[18] M. İlhan, M.K. Ekmekçi, J. Solid. State. Chem. 226 (2015) 243–249.
[19] D. Zhang, X. Meng, Y. Meng, X. Pu, B. Ge, W. Li, J. Dou, Sep. Purif. Technol. 186 (2017) 282–289.
[20] M. İlhan, J. Therm. Anal. Calorim. 147 (2022) 12383–12389.
[21] M. İlhan, M.K. Ekmekçi, İ.Ç. Keskin, RSC Adv. 11 (2021) 10451–10462.
[22] A.S. Başak, M.K. Ekmekçi, M. Erdem, M. İlhan, A. Mergen, J. Fluoresc. 26 (2016) 719–724.
[23] E.K. Akdogan, R.E. Brennan, M. Allahverdi, A. Safari, J. Electroceram. 16 (2006) 159–165.
[24] M. Thirumal, P. Jain, A.K. Ganguli, Mater. Chem. Phys. 70 (2001) 7.
[25] M.K. Ekmekçi, M. İlhan, A. Ege, M. Ayvacıklı, J. Fluoresc. 27 (2017) 973–979.
[26] Z. Song, J. Ma, H. Sun, Y. Sun, J. Fang, Z. Liu, C. Gao, Y. Liu, J. Zhao, Mater. Sci. Eng. B 163 (2009) 62–65.
[27] M. İlhan, İ.Ç. Keskin, Dalton Trans. 47 (2018) 13939–13948.
[28] M. Sato, Y.J. Hama, J. Solid State Chem. 118 (1995) 193–198.
[29] W. Wong-Ng, H.F. McMurdie, B. Paretzkin, Y. Zhang, K.L. Davis, C.R. Hubbard, A. L. Dragoo, J.M. Stewart, Powder Diffr. 2 (1987) 191–202.
[30] İ.Ç. Keskin, M. Türemiş, M.İ. Katı, S. Gültekin, Y.T. Arslanlar, A. Çetin, R. Kibar, J. Lumin. 225 (2020), 117276.
[31] S. Ilican, F. Yakuphanoglu, M. Caglar, Y. Caglar, J. Solid. State. Electrochem. 509 (2011) 5290–5294.
[32] M.L. Addonizio, C. Diletto, Sol. Energy Mater. Sol. Cells 292 (2022), 126649.
[33] R.B.H. Tahar, N.B.H. Tahar, J. Mater. Sci. 40 (2005) 5285–5289.
[34] D. Chen, D. Yang, Q. Wang, Z. Jiang, Ind. Eng. Chem. Res. 45 (2006) 4110–4116.
[35] A. Nakamura, N. Nambu, H. Saitoh, Sci. Technol. Adv. Mate. 6 (2005) 210–214.
[36] W.E. Moddeman, A.R. Burke, W.C. Bowling, D.S. Foose, Surf. Interface Anal. 14 (1989) 224.

[37] D.H. Quinones, A. Rey, P.M. Álvarez, F.J. Beltrán, G.L. Puma, Appl. Catal. B 178 (2015) 74–81.
[38] W. Zhang, T. Hu, B. Yang, P. Sun, H. He, J. Adv. Oxid. Technol. 16 (2013) 261–267.
[39] Y.J. Hsiao, Y.S. Chang, G.J. Chen, Y.H. Chang, J. Alloys Compd. 471 (2009) 259–262.
[40] Y.J. Hsiao, T.H. Fang, L.W. Ji, S.S. Chi, Open Surf. Sci. J. 1 (2009) 30–33.
[41] M.K. Ekmekçi, M. Erdem, A. Mergen, G. Özen, B.D. Bartolo, J. Alloys Compd. 591 (2014) 230–233.
[42] Q. Shao, H. Zhang, J. Dai, C. Yang, X. Chen, G. Feng, S. Zhou, Cryst. Eng. Comm. 21 (2019) 741–748.
[43] Y. Kim, S. Kang, Acta Mater. 59 (2011) 3024–3031.
[44] J. Shan, M. Uddi, R. Wei, N. Yao, Y. Ju, J. Phys. Chem. C 114 (2010) 2452–2461.
[45] J.Y. Park, H.C. Jung, G.S.R. Raju, B.K. Moon, J.H. Jeong, S.M. Son, J.H. Kim, Opt. Mater. 32 (2009) 293–296.
[46] G.S.R. Raju, S. Buddhudu, Mater. Lett. 62 (2008) 1259–1262.
[47] M. İlhan, İ.Ç. Keskin, L.F. Güleryüz, M.İ. Katı, J. Mater. Sci.: Mater. Electron. 33 (2022) 16606–16620.
[48] J.W. Stouwdam, F.C.J.M. van Veggel, Nano Lett. 2 (2002) 733–737.
[49] C.S. McCamy, Color Res. Appl. 17 (1992) 142–144.